

FRACTURE ANALYSIS OF POROUS BIO CERAMICS BY FINITE ELEMENT METHOD

TAKA AKI ARAHIRA¹, MITSUGU TODO² AND AKIRA MYOUI³

¹Faculty of Management and Information Sciences
Kyushu Institute of Information Sciences
6-3-1, Saifu, Dazaifu, Fukuoka 818-0117, Japan
arahira@kiis.ac.jp

²Research Institute for Applied Mechanics
Kyushu University
6-1, Kasuga-koen, Kasuga, Fukuoka 816-8580, Japan
todo@riam.kyushu-u.ac.jp

³Department of Medical Innovation
Osaka University Hospital
2-2, Yamadaoka, Suita, Osaka 565-0871, Japan
myoi@hp-mctr.med.osaka-u.ac.jp

Received November 2020; accepted February 2021

ABSTRACT. *In recent years, much attention has been paid to tissue engineering for bone regeneration. In current orthopedic treatments, artificial bone substitutes composed of bioactive ceramics are sometimes used instead of autografts and allografts to obtain bone tissue ingrowth in damaged regions. In this study, the fracture mechanism of nonabsorbable porous hydroxyapatite was assessed using 3D finite element analysis (FEA). 3D finite element (FE) models were constructed using μ -CT images of porous hydroxyapatite. Computational analysis was conducted under compressive loading. The elements of both tensile and compressive fracture increased as the value of the compressive load increased. This study showed the potential for applying the computational method to evaluating the time-dependent fracture process of porous bioceramics.*

Keywords: 3D-CT FEM, Artificial bone substitute, Bioactive ceramics, Fracture analysis

1. Introduction. The spontaneous recovery of bone tissue after large-scale damage caused by an osteoma or periprosthetic bone resorption around an artificial joint is very difficult. To ensure bone tissue regeneration, a therapeutic intervention that aids the healing process is needed. In recent years, the application of porous artificial bone with high bone affinity and osteoconductivity has been investigated [1-3] and has progressed to clinical application [4-6]. Bioceramics are often used as porous artificial bones; however, the injury and fracture behavior of artificial bones with porous structures are difficult to investigate in detail due to their structural complexity.

On the contrary, with the recent developments in computational mechanics, it has become possible to construct a detailed 3D FE model using CT images [7-9]. Hence, it is expected that a more detailed understanding of the mechanical behavior can be obtained by performing μ -CT-based numerical analysis in addition to μ -CT-based structural assessment, which is one of the methods currently being used for material evaluation in vivo experiments. Recent studies have been conducted using numerical analysis of the scaffold μ -CT images [10,11] and comparing its results with the experimental results [12-15]. Hence, the incorporation of fracture criteria into numerical analysis is expected to

facilitate detailed studies on the injury/fracture mechanisms of porous artificial bone, which is usually difficult in an experimental setting.

This study was aimed at clarifying the fracture behavior of porous artificial bone by creating a numerical model of HA artificial bone. This model reproduces a continuous porous structure using μ -CT images, which enables to perform numerical analysis using the finite element method (FEM) together with a fracture model.

2. Materials and Methods.

2.1. Materials. The porous HA artificial bone, NEOBONE[®], was used for the numerical analysis. It has an average pore diameter of 150 μm and an interconnected structure suitable for tissue invasion. Figure 1(A) shows an SEM image of this artificial bone.

2.2. Experimental procedure. To determine the compressive strength, we conducted a compression test on the NEOBONE[®] specimens at a displacement speed of 1 mm/min using a small-size material testing device and then recorded the load-displacement relationship [3]. The obtained load and displacement values were converted into stress and strain values, respectively. After creating the stress-strain diagrams, the maximum load value in the initial linear elastic region was defined as the compressive strength value. Figure 1(B) shows the stress-strain curve of the NEOBONE[®]. The stress increased linearly from the start of the compression test and became nonlinear around the strain value of 0.04. The stress decreased after reaching the maximum stress value. This stress-strain curve showed that the compressive strength was 16.2 MPa. Because the length of one of the sides of the NEOBONE[®] was 10 mm whereas that of the analytical model was 0.5 mm, we corrected the size and set the load of the analytical model to 4.05 N for the analysis.

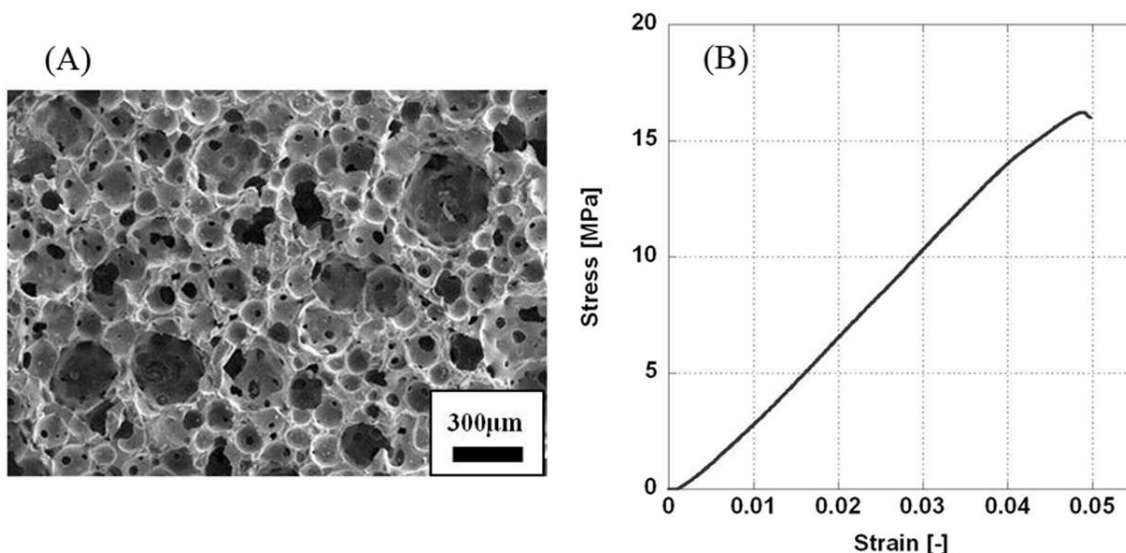


FIGURE 1. The experimental results of NEOBONE[®]. (A) is SEM image, and (B) is compressive stress-strain curve, respectively.

2.3. Modeling and analysis. We created a cube-shaped model with 0.5 mm sides using the μ -CT images of artificial bones. We used Mechanical Finder, a biological structure analysis software, for modeling and analysis. The slice interval of μ -CT was 0.01 mm. Figures 2(A) and 2(B) show the solid and mesh diagrams of the artificial bone model.

The FEA reproduced the fracture behavior of the NEOBONE[®]. We used the maximum principal stress as a criterion for tensile failure and the minimum principal strain as a criterion for compressive failure. The stiffness of the maximum principal stress method

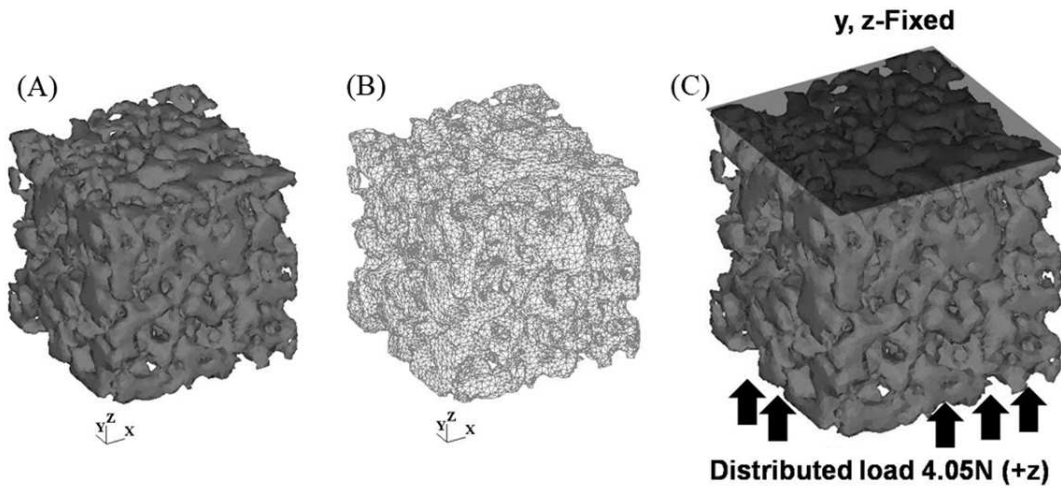


FIGURE 2. Computational modeling design. (A) is 3D solid model, (B) is 3D mesh model, and (C) is boundary condition, respectively.

was set to zero when the maximum principal stress value reached the tensile failure reference value in a certain element, and it was assumed that the fractures occurred in a direction perpendicular to the direction of the maximum principal stress. Contrarily, the stiffness matrix element was set to zero, assuming that the element is fractured when the minimum principal strain value reached the compressive failure reference value. A compression test was performed in the boundary conditions for the analysis by fixing the upper part in the y and z directions and applying a distributed load of 4.05 N from the lower part to the lead vertical direction ($+z$ direction) (Figure 2(C)). The Young's modulus of the model was set uniformly to 1077 MPa and the Poisson's ratio was set to 0.4. The Young's modulus of this model is the maximum value in the model considering the Young's modulus distribution. An analysis was performed without considering the fracture, and from the obtained results, the average maximum principal stress and average minimum principal strain were obtained. These values were used as a reference value for the tensile and compressive failure, respectively.

3. Main Results. The maximum principal stress and minimum principal strain distributions obtained from the compression analysis are shown in Figures 3 and 4, respectively. The maximum principal stress is a tensile stress, whose concentration was confirmed near the bone pores. The principal stresses were confirmed to be distributed more broadly inside the sample from the central cross-section. On the contrary, the minimum principal strain is a compressive strain, wherein the strain concentration was confirmed to occur at a relatively narrow skeleton area from the central cross-section. From the above results, we calculated the mean values of the maximum principal stress and minimum principal strain in the model and found them to be 8.7 MPa and -0.042 , respectively. Furthermore, the fracture analysis was attempted by setting these as the critical values for tensile and compressive failure, respectively.

Figures 5 and 6 show the results of the fracture analysis, including the distributions for each load value of the maximum principal stress and minimum principal strain, respectively. The number of stress concentration locations increased as the load value increased. Furthermore, at 2 N, the regions of tensile fracture shown in red were expanded in the central cross-section. The minimum principal strain also experienced similar expansion in the concentration regions as the load value increased. The models indicating the tensile and compressive fracture elements are shown in Figures 7 and 8, respectively. Additionally, the number of tensile and compressive fracture elements at each load value are summarized in Table 1. The tensile fracture, but not the compressive fracture, occurred

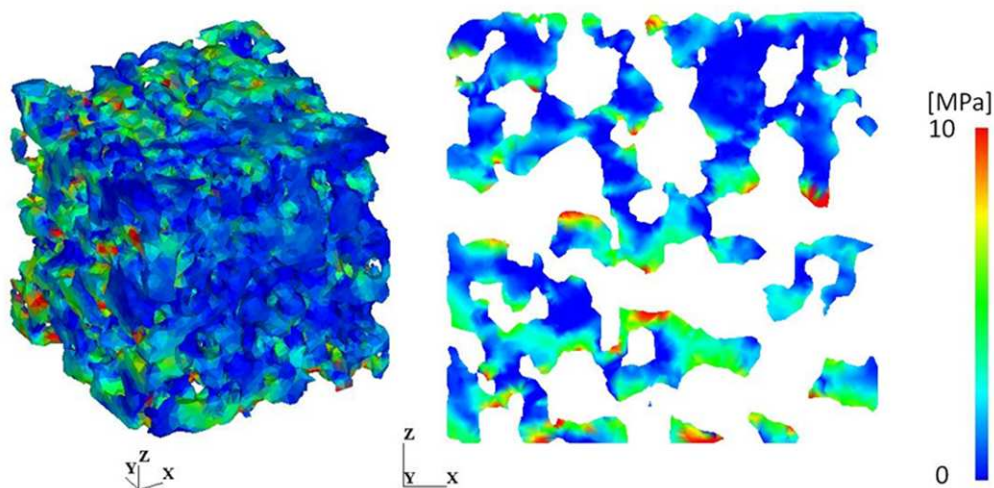


FIGURE 3. (color online) Distribution of maximum principal stress

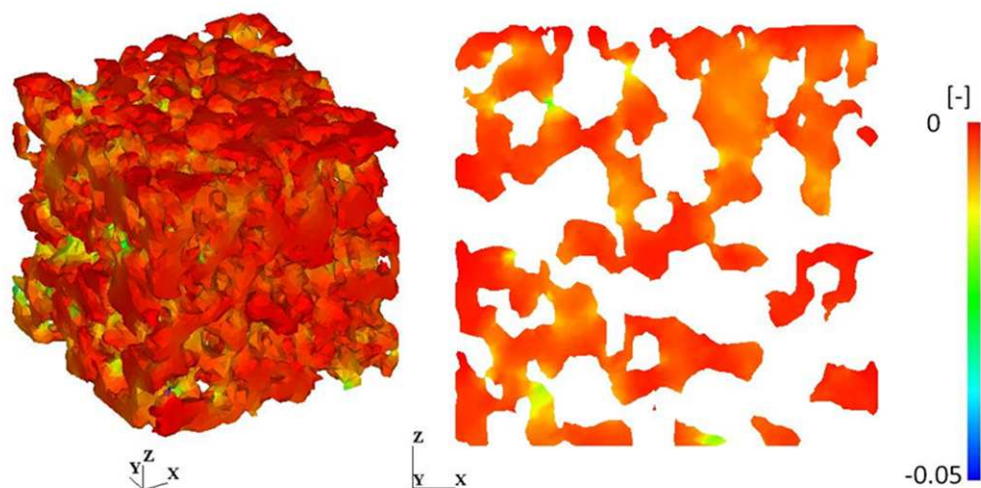


FIGURE 4. (color online) Distribution of minimum principal stress

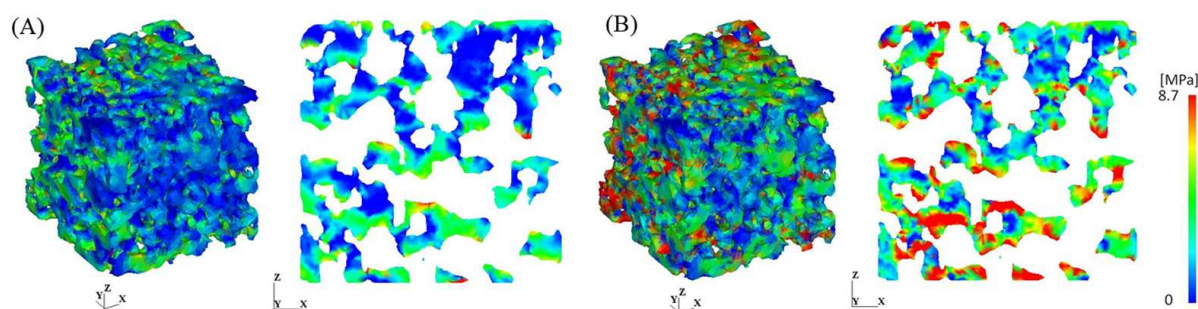


FIGURE 5. (color online) Distribution of maximum principal stress under fracture analysis. (A) is 1 N, and (B) is 2 N, respectively.

at 1 N. In addition to the occurrence of a compressive fracture, the number of tensile and compressive fracture elements increased about ten times at 2 N than at 1 N.

4. Discussion. In this analysis, we performed compression tests on actual samples and set load conditions based on the compression strength. It is preferable to conduct the numerical analysis under the same conditions as those used in the experimental analysis to reproduce the changes in the mechanical behavior that cannot be obtained in detail using

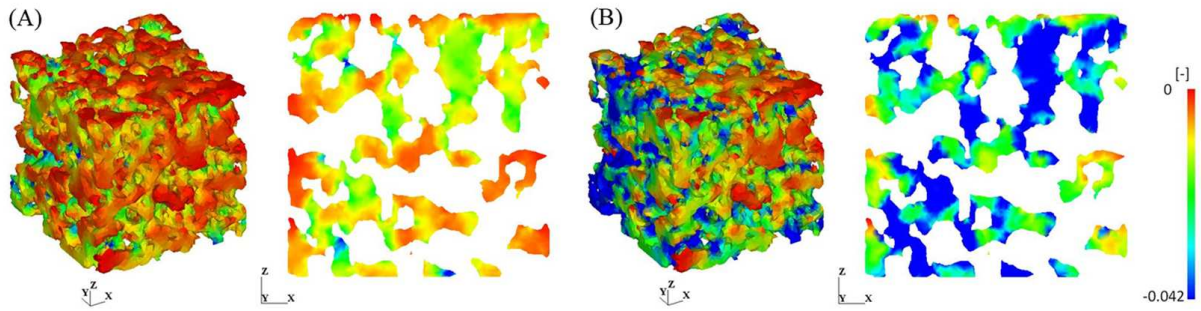


FIGURE 6. (color online) Distribution of minimum principal stress under fracture analysis. (A) is 1 N, and (B) is 2 N, respectively.

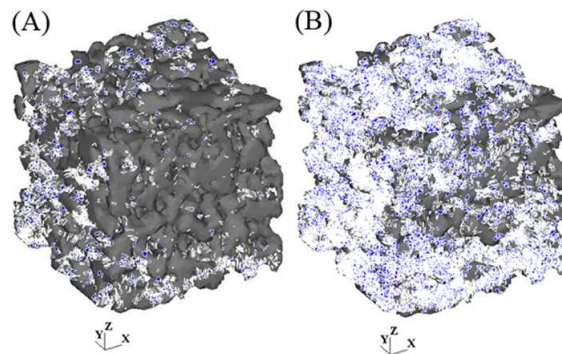


FIGURE 7. (color online) Distribution of elements of tensile fracture. (A) is 1 N, and (B) is 2 N, respectively.

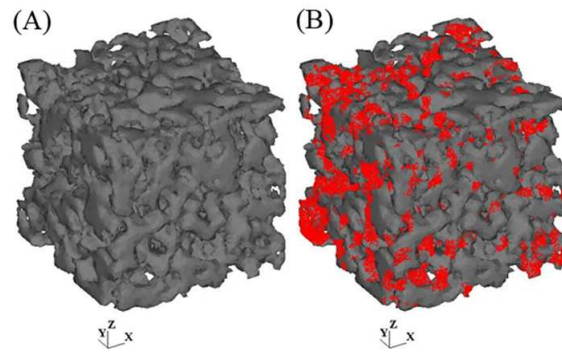


FIGURE 8. (color online) Distribution of elements of compressive failure. (A) is 1 N, and (B) is 2 N, respectively.

TABLE 1. Element numbers of tensile fracture and compressive failure

Load	Tensile fracture	Compressive failure
1 N	19803	0
2 N	117113	47009

the experimental results. First, we discuss the results of the analysis without considering fracture. The maximum principal stress distribution was broadly concentrated near the pores, whereas the minimum principal strain distribution was mainly concentrated in the narrow skeletal areas. Considering this, although the compressive strains occur at the narrow part of the skeleton, it can be assumed that the surrounding area is subjected to the tensile forces. Comparing the distributions between the maximum principal stress

and minimum principal strain across the central cross-section, the principal stress concentration is confirmed to occur around the strain concentration in the narrow part of the skeleton.

For the fracture analysis, the maximum load value was set to 4.05 N; however, the analysis ended at 2 N. We assumed that the element's destruction occurred throughout the model and the element was no longer able to support the load. As for the maximum principal stress distribution, the number of stress concentration locations increased as the load values increased. Similarly, the minimum principal strain also expanded in the concentration region as the load value increased. In particular, it was suggested that the progression of compressive fracture occurs in the same location because the strain concentration post-compression occurred in the narrow part of the skeleton. In addition, considering the number of fracture elements, it is thought that the compressive failure may have occurred as the tensile failure progressed. This may have occurred because the number of compressive fracture elements was zero at a load value of 1 N, but increased at 2 N, and the number of tensile fracture elements was confirmed at 1 N. However, the boundary conditions require a more detailed examination to reproduce the actual fracture behavior because the analysis itself was completed at a load value of 2 N. Furthermore, in this analysis, only one part of the μ -CT image was extracted and modeled, suggesting that the fracture behavior can be reproduced in more detail by conducting a similar analysis with multiple models extracted from multiple locations.

5. Conclusions. In this analysis, we performed compression tests on actual samples and set load conditions based on the result of compression test. It was concluded that the detailed fracture behavior of NEOBONE[®] could be reproduced using a nonlinear FEA method by introducing models of maximum principal stress-based tensile fracture and minimum principal strain-based compressive fracture. In the future, the result of this study should be compared with experimental data in vivo to assess the relationship between mechanical property and material fracture behavior.

Acknowledgment. The authors thank Crimson Interactive Pvt. Ltd. (Ulatas) – www.ulas.jp for their assistance in manuscript translation and editing.

REFERENCES

- [1] O. Gauthier, R. Müller et al., In vivo bone regeneration with injectable calcium phosphate biomaterial: A three-dimensional micro-computed tomographic, biomechanical and SEM study, *Biomaterials*, vol.26, pp.5444-5453, 2005.
- [2] M. Motomiya, M. Ito et al., Effect of Hydroxyapatite porous characteristics on healing outcomes in rabbit posterolateral spinal fusion model, *European Spine Journal*, vol.16, pp.2215-2224, 2007.
- [3] N. Yamasaki, M. Hirao et al., A comparative assessment of synthetic ceramic bone substitutes with different composition and microstructure in rabbit femoral condyle model, *Journal of Biomedical Materials Research – Part B*, vol.91, pp.788-798, 2009.
- [4] M. Marcacci, E. Kon et al., Stem cells associated with macroporous bioceramics for long bone repair: 6- to 7-year outcome of a pilot clinical study, *Tissue Engineering*, vol.13, pp.947-955, 2007.
- [5] M. Matsuo, T. Sugita et al., Rigid bridging of massive femur defect using double vascularized fibula graft with hydroxyapatite, *Archives of Orthopaedic and Trauma Surgery*, vol.128, pp.941-944, 2008.
- [6] Y. Yoshida, S. Osaka et al., Clinical experience of novel interconnected porous hydroxyapatite ceramics for the revision of tumor prosthesis: A case report, *World Journal of Surgical Oncology*, vol.7, 2009.
- [7] T. Arahira, M. Todo et al., Assessment of mechanical stability and safety for fully edentulous maxilla with dental implants, *Journal of Solid Mechanics and Materials Engineering*, vol.4, pp.953-962, 2010.
- [8] T. Arahira, M. Todo et al., Biomechanical analysis of implant treatment for fully edentulous maxillas, *Journal of Biomechanical Science and Engineering*, vol.5, pp.526-538, 2010.
- [9] Q. H. Zhang, J. Y. Wang et al., A subject-specific pelvic bone model and its application to cemented acetabular replacements, *Journal of Biomechanics*, vol.43, pp.2722-2727, 2010.

- [10] C. Landsberg, F. Stenger et al., Chemotaxis of mesenchymal stem cells within 3D biomimetic scaffolds – A modeling approach, *Journal of Biomechanics*, vol.44, pp.359-364, 2011.
- [11] E. Askari, I. F. Cengiz et al., Micro-CT based finite element modelling and experimental characterization of the compressive mechanical properties of 3-D zirconia scaffolds for bone tissue engineering, *Journal of the Mechanical Behavior of Biomedical Materials*, vol.102, 103516, 2020.
- [12] L. Freitag, C. Günther et al., Relative effects of age on implant integration in a rat model: A longitudinal in vivo microct study, *Journal of Orthopaedic Research*, vol.37, no.3, pp.541-552, 2019.
- [13] J. A. NacNeil and S. K. Boyd, Bone strength at the distal radius can be estimated from high-resolution peripheral quantitative computed tomography and the finite element method, *Bone*, vol.42, pp.1203-1213, 2008.
- [14] L. M. Ren, M. Todo et al., A comparative biomechanical study of bone ingrowth in two porous hydroxyapatite bioceramics, *Applied Surface Science*, vol.262, pp.81-88, 2012.
- [15] L. M. Ren, T. Arahira et al., Biomechanical evaluation of porous bioactive ceramics after implantation: Micro CT-based three-dimensional finite element analysis, *Journal of Materials Science: Materials and Medicine*, vol.23, pp.463-472, 2012.